From the bulge region to the outer disk: Tracing the α-enhancement level in the Galactic thin and thick disks

Elin Sandvik

Lund Observatory
Lund University

Abstract

One of the biggest mysteries astronomers wish to unveil is the formation and evolution of galaxies. Properties of our own galaxy, the Milky Way, can provide great insight into these. The star formation rate (SFR) and whether it varies with distance from the galactic centre (GC), is one of these properties. Studies indicate that the SFR is higher in the bulge region than in the local thick disk of our galaxy. One would expect it to continue to decrease outwards since the gas density is lower further away from the GC.

This thesis aims to trace the SFR "knee", which is an indication of SFR when analysing the α-element abundances of a star. In this study, we will investigate if the knee's position changes for stars residing in different regions of the Milky Way.

To trace the position of the knee, generalised Gaussian distributions were constructed for the α-element abundances in different [Fe/H] intervals. The peaks of these could then be used to pinpoint where the star-count was largest in each metallicity interval. The knee appears most prominent in the [Mg/Fe] abundance trend, which was therefore chosen as the focus of the analysis. Data from APOGEE DR16 will be used, which also contains Bailer-Jones distance estimates from Gaia DR2.

Stars believed to have originated from mergers were excluded. These are not of interest since the study only wishes to trace the α-abundance trends of the Milky Way itself. Furthermore, to avoid any selection bias, only giants were included, since dwarfs are intrinsically fainter and difficult to observe at greater distances.

The results found that the knee in the abundance trends of [Mg/Fe] with [Fe/H] seemed shifted to higher metallicities towards the GC, which implies a varying SFR throughout the Milky Way. However, this shift is only found if we look at the shift of the slope itself. Previous studies have also found that the bulge region has elevated [α/Fe] abundances at higher [Fe/H], compared to the local thick disk. An estimated shift of [Fe/H]$\approx +1.0$ was found, in accordance with the results of other studies. The results also found that the IMF appeared larger in the bulge region than in the local thick disk.

In conclusion, the study found that the bulge region could have had a higher SFR and IMF than the local thick disk. These are indicators that they are separate components, and that the bulge region is not solely a superposition of thick disk, thin disk, halo, and bar components. Instead, it could be a separate component with its own stellar population.

Populärvetenskaplig beskrivning

I vårt stora, komplexa universum är det uppskattat att det finns ungefär två biljoner galaxer. Just vår hemgalax, Vintergatan, ligger mellan de två typiska galaxpopulationerna, i den så kallade "gröna dalen". Galaxer i den gröna dalen är i en fas mellan att aktivt bilda stjärnor och att vara döda. I och med detta så kan vi lära oss mycket om galaxers utveckling genom att studera Vintergatan och dess egenskaper.

Något som är viktigt att bestämma är stjärnbildningshastigheten, d.v.s. hur snabbt nya stjärnor föds från stjärnstoftet i galaxen. Ju tätare gasen är, desto fler stjärnor bildas. Vid något tillfälle i ens liv brukar man få höra att vi alla är gjorda av stjärnstoft. Detsamma gäller även för stjärnorna själva, som föds från det material döda stjärnor tillverkat. I och med att gasen är som tätast i Vintergatans center och minskar allteftersom man närmar sig galaxens utkant, så förväntas stjärnbildningshastigheten avta längre ut.

Det som man sett är att den tjocka disken, om den existerar inne i Vintergatans centrala region (d.v.s. bulgen), verkar vara aningen mer anrikad i alfa-grundämnen än vad man observerar i den tjocka disken i solens närhet. Det är oklart vad det beror på, eller om det ens är riktigt att så är fallet. Detta projekt går ut på att undersöka det.

Ett tillvägagångssätt att uppskatta stjärnbildningshastigheten på är att jämföra trender för alfa-grundämnen med järnhalter. Alfa-grundämnen tillverkas bara av massiva stjärnor, medan järn tillverkas av stjärnor av alla storlekar. När stjärnor dör i supernovaexplosioner så skickas dessa ämnen ut och berikar gasen i galaxen. Små stjärnor lever betydligt längre än massiva stjärnor, vilket betyder att det tar längre tid innan galaxen blir berikad av järngas från de små stjärnorna. När detta väl sker så ändras förhållandet mellan alfa-grundämnen och järn i gasen som nya stjärnor bildas av. Det innebär att unga stjärnor har högre järnhalter och lägre alfa-grundämneshalter, jämfört med äldre stjärnor.

Som ett resultat av detta så uppkommer ett "knä" i fördelningen av stjärnor när man undersöker deras alfa-grundämneshalter med järnhalter. Det alfa-grundämnet som ger upphov till ett mer markant knä än de andra är magnesium. Därmed så valdes magnesium som fokuspunkt i analysen. Beroende på hur hög järnhalten är när knäet framstår så kan man uppskatta den relativa stjärnbildningshastigheten mellan olika regioner.

I detta projekt framgick det som att stjärnbildningshastigheten möjligtvis är högre närmre Vintergatan mittpunkt än i solens närhet. Detta stämmer överens med tidigare studier och är alltså ytterligare en indikation att det kan stämma. Huruvida detta resultat är påverkat av faktorer så som stjärnors rörelser inåt eller utåt i galaxen är svårbesvarade, men viktiga, frågor.

Contents

List of Figures

List of Tables

Chapter 1

Introduction

Residing in the green valley, with the morphology of an SBbc type (or potentially earlier (SBb) due to its high bulge mass (Barbuy et al. 2018)), our home, the Milky Way, is a benchmark galaxy of its kind. Its properties can provide us with great knowledge regarding galaxy formation and evolution. As the green valley is situated between the two populations of galaxies, the blue cloud and the red sequence (Bland-Hawthorn & Gerhard 2016), the Milky Way's properties can shed light on details regarding the transition between an active and a dead galaxy. These details include properties such as star formation, gas flows and nucleosynthesis (Matteucci 2003).

The Milky Way is typically divided into four parts: the central bulge, the thin and thick disks, and a spherical halo. The two disks differ in the aspect of stellar populations; the thin disk typically contains younger stars, whereas the thick disk consists of older stars (Edvardsson et al. 1993; Bensby et al. 2014). Originally, it was unsure whether our galaxy had more than one disk (Bovy et al. 2012), whereas some claimed it had two, or possibly even three (Lee et al. 2011; Liu & van de Ven 2012). Recent data of high precision indicate that the scenario of two disks seems more plausible (Bensby et al. 2014).

A recent study by Barbuy et al. (2018) suggested that the thick disk and bulge are two different components, and that the bulge region is not just a superposition of halo, thick-disk, thin-disk, and bar components. This study therefore also wishes to bring some clarity to whether this is the case, by examining the abundance trends for $[\alpha/\text{Fe}]$ with $[\text{Fe/H}]$ in different regions of the Milky Way. In particular, to examine if the initial mass function (IMF) and star formation rate (SFR) are larger for the bulge region compared to the local thick disk. If such is the case, it would indicate that the bulge and thick disk are separate components in the Milky Way.

The variation of chemical abundances throughout the galaxy can be used to estimate the SFR. Stars typically have varying chemical compositions depending on their age, which can be estimated by their α-element abundances. Through using their position on an Hertzsprung-Russell diagram and analysing where a given star then resides on an $[\alpha/\text{Fe}]$ versus $[\text{Fe/H}]$ plot, studies have found that older stars typically have a higher α-element abundances (see e.g. Bensby et al. 2003; Snaith et al. 2015). When analysing the relation between $[\alpha/\text{Fe}]$ and $[\text{Fe/H}]$, a "knee" in the trend for the thick disk stars become evident.

6
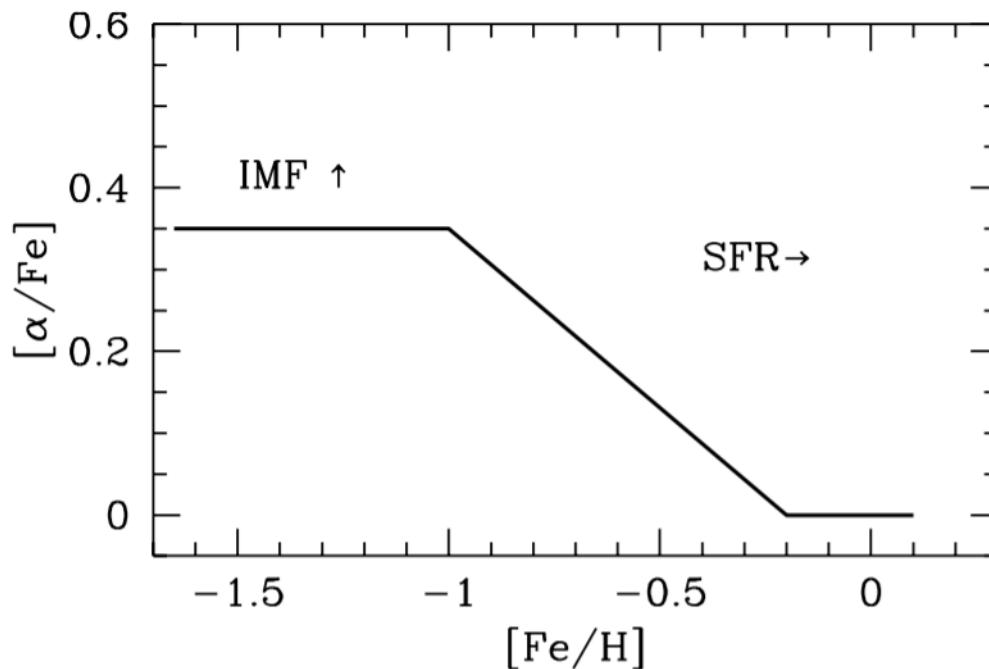
Figure 1.1: An illustration of the α-element abundance trend with metallicity. The arrows indicate how the trend changes with an increasing IMF or SFR (McWilliam 1997).

This knee is illustrated in figure 1.1, and its position is an indication of SFR. The level of the α-enhancement and the position of the knee is what will be analysed in this thesis and the aim is to examine whether it changes its position in [Fe/H] for different galactocentric distance intervals.

This can provide insight into the SFR of the thick disk, whether or not it is constant with increasing distance from the GC, and furthermore how it may be connected to stars residing in the central bulge region. Recent studies have seen that the bulge abundance trends are somewhat elevated at higher metallicities, compared to those in the local thick disk samples (Bensby et al. 2013, 2017; Johnsson et al. 2014; Jönsson et al. 2017; Rojas-Arriagada et al. 2017).

The disk to be studied in detail in this thesis is the thick disk, along with the bulge. The former contains older stars (Adibekyan et al. 2011; Bensby et al. 2014) of wider α-element abundance variations, giving rise to a more prominent knee in the [α/Fe] to [Fe/H] relationship. Stars residing in the bulge span a wide range of ages (Bensby et al. 2017), and are thus also of interest for the analysis. The thin disk's abundance trends will be examined as well.

A knee positioned at higher metallicities in the [α/Fe] trends would indicate a larger SFR, as indicated in figure 1.1 (McWilliam 1997). In the figure, the IMF is also indicated. High-mass stars are the ones which produce α-elements, which results in an elevated α-element abundance level. If more of high-mass stars are formed, it would result in a

larger IMF in the investigated region. The knee is due to the onset of type Ia supernovae (SNIa), which only enriches the interstellar medium (ISM) with iron, and no α-elements (McWilliam 1997). Before SNIa explosions occur, the ISM is primarily enriched by α-elements and iron from type II supernovae (SNII), giving rise to the plateau seen in figure 1.1 before the knee.

If the analysis finds a shift in the position of the knee in the thick disk's α-abundance trends, it might indicate that the SFR varies throughout the Milky Way. This would confirm the results from previous studies (e.g. Bensby et al. 2017; Bensby et al. 2013; Johnsson et al. 2014; Jönsson et al. 2017; Rojas-Arriagada et al. 2017), which have found that the bulge appeared to have elevated α-element trends at higher metallicities compared to the local thick disk.

If the SFR knee remains at a constant metallicity, it would contradict studies which have found that the galaxy gas density decreases radially (Hiroyuki & Yoshiaki 2016). Since gas density has a major impact on the SFR, it follows that the SFR should also decrease towards the outer edge of the Milky Way. A smaller SFR would position the knee at lower metallicities in the α-element abundance trends. However, both results are interesting on their own, since it is not until recently that studies have indicated elevated α-element abundances in the bulge region.

Although many studies investigate the chemical composition, evolution, and SFR of the Milky Way and other galaxies, none seem to focus solely on mapping the SFR knee. The results of this thesis will be useful for studying the overall structure and evolution of the Milky Way. Whether the bulge region is a separate component, and not just a superposition of the thin disk, thick disk, halo, and bar components, can be interpreted from the differences in IMF and SFR between the bulge region and local thick disk. Even if it sheds light to whether the SFR might vary or not throughout our galaxy, the results will pose further questions, such as whether radial migration has had an impact on the interpreted SFR. However, there is currently no way for us to know exactly how it might have influenced the results.

In chapter 2, we present how the data was selected and how a clean disk sample was ensured, such that the analysis would focus solely on stellar components of the disks. There, we also present how selection bias was avoided by excluding dwarfs from the sample. Details regarding how the thin and thick disks' trends were traced using generalised Gaussian distributions are presented in chapter 3, as well as how the error analysis using bootstrapping was done. The results of the analysis and bootstrapping are presented in chapter 4. The findings are then discussed in chapter 5, from which we draw conclusions in chapter 6.

Chapter 2

Data

2.1 The APOGEE DR16 sample

The study will be conducted through analysing data from the recent data release APOGEE DR16 (SDSS-IV Collaboration 2019), which stands for Apache Point Observatory Galaxy Evolution Experiment Data Release 16. It is a large spectroscopic survey aimed to obtain detailed elemental abundances and radial velocities of hundreds of thousands of stars throughout the Milky Way. The data release contains a huge variety of properties for 473 307 stars. Some information is not available for certain stars, which means that each quantity used in the algorithm will constrain the data set further.

Some stars belong to dwarf Spheroidal satellites (dSph), the Sagittarius system, star clusters, Magellanic clouds, or stellar streams. This is because APOGEE specially targeted these streams and structures. Since the goal is to study the stellar components of the Milky Way, these need to be excluded from the sample. Furthermore, there are stars in the sample with poor quality, such as warnings on elemental abundances, effective temperature, self-gravity, or if measurements were flawed in other ways. Since the data set is huge, and many stars can be of poor quality, these should also be excluded from the analysis. Examples of these poor qualities are stars with a much brighter neighbour, if the spectrum has bad pixels, or if parameters for i.e. chemical compositions are flawed. The APOGEE data set contains flags for these stars, and they could thus be filtered out from the code. Once excluded, the remaining sample size was down to 203 313 stars.

The distance estimates found in APOGEE DR16 are Bailer-Jones estimates from Gaia DR2 (Gaia Collaboration et al. 2018). The data set already contains parallaxes of each star, but reliable distance estimates cannot be derived from simply inverting these. Bailer-Jones accounts for the non-linearity of the transformation, as well as the asymmetry of the probability distribution (Bailer-Jones et al. 2018). As is noted in Bailer-Jones et al. 2018, some stars' distance estimates can be improved by using additional data, such as photometry. However, the goal of Bailer-Jones is to have purely geometric distance estimates, which means that other data is not accounted for.

The distribution of the remaining sample of 203 313 stars in the galaxy can be seen
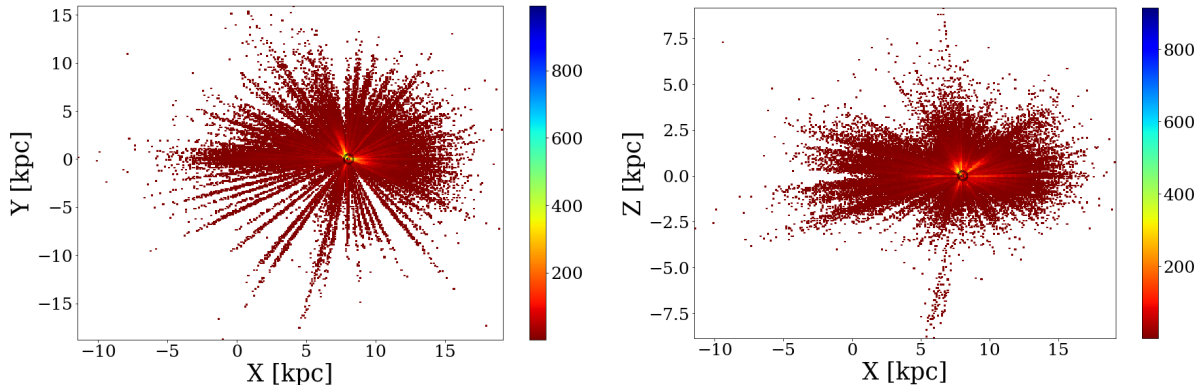
Figure 2.1: The distribution of stars in the sample given in kpc for the galactocentric frame, where ⊙ indicates the Sun's position. The left figure shows the distribution seen face-on, and the right figure shows it edge-on.

in figure 2.1. Here, the observational bias is evident, seeing as the star number density is highest in the solar vicinity. For an ideal comparison, the sample size would be similar in each galactocentric radius region. The Sun's position in these figures is marked with ⊙.

The study wished to look at the different galactocentric distance intervals of 0-4 kpc, 4-7 kpc, 7-9 kpc, and 9-12 kpc. The bulge is believed to stretch out to at least 4 kpc, which motivates the first choice of interval. The region of 7-9 kpc is the solar neighbourhood, which is desirable to study and compare to previous studies of the local thick disk and bulge abundance trends. The region between these, 4-7 kpc, is also of interest to include since it shows how the trends look between the bulge and the solar vicinity. Lastly, the 9-12 kpc region is the outer neighbouring region to the local thick disk. Since we are primarily interested in comparing the α-enhancement of the local thick disk and the bulge region, this limit is sufficient for the analysis.

The distances state approximately how far away a star is from the Sun. Therefore, these need to be expressed in terms of galactocentric distance instead. They were converted to the galactocentric frame using `astropy.SkyCoord`.

There are many different α-element abundances which are interesting to investigate, and show a clear knee in the trend when plotted against the metallicity. However, one element stands out among these, and that is the magnesium abundances. Mg has a distinct separation between the thin and thick disk, whereas other α-elements overlap more between the two disks, increasing the difficulty of a successful analysis. Additionally, Mg also has a steeper gradient for the knee, in contrast to most α-elements. The star distribution for Mg can be seen in figure 2.2, and the ones for Si and Ca can be seen in appendix A and B, in figures A.1 and B.1. It is worth noting that, unless explicitly stated otherwise, the colour bars on the density plots describe how many stars are present in the bins.
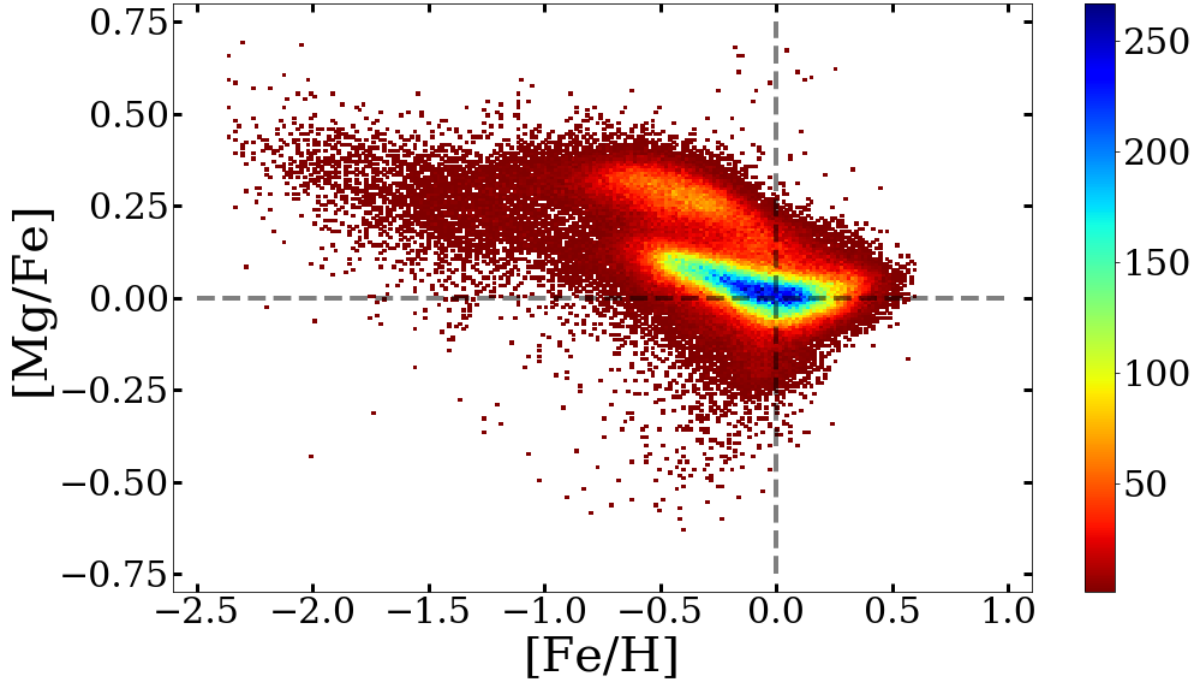
Figure 2.2: The star distribution for [Mg/Fe] versus [Fe/H] for the 203 313 stars in the sample.

2.2 Creating a clean disk sample

A factor that could alter the results is the presence of accreted stars, from a merger with e.g. the Gaia-Enceladus dwarf galaxy. The Gaia-Enceladus merger with the Milky Way brought with it stars and elemental abundances which do not originate from our own galaxy. Those stars are believed the be the tail and spread behind the thick and thin disk seen in figure 2.2, starting at around -0.5 [Fe/H] dex and stretches to lower metallicities. For a light element like Mg, the scatter seen should reflect the effects of enrichment and mixing from early merger events in the Milky Way's history (Arnone et al. 2005).

In an attempt to remove the scattered stars, a constraint was put on the model using the [Al/Mg] distribution with [Mg/H], seen in figure 2.3a. By manually excluding the tail seen in this trend, such that the constrained distribution is as seen in figure 2.3b (Diane Feuillet, private communication), many of the scattered stars could be excluded. This proved to be successful, and the stars which were now excluded from the [Mg/Fe] with [Fe/H] distribution can be seen in figure 2.4. The stars which now remained in the sample, for different α-elements and galactocentric distances, can be seen in the middle row of figure 2.6. To see the impact this constraint has on Si and Ca, we refer to figures A.2 and B.2, respectively, in the appendix.

(a) Full [Al/Mg]-[Mg/H] distribution.   (b) Constrained [Al/Mg]-[Mg/H] distribution.
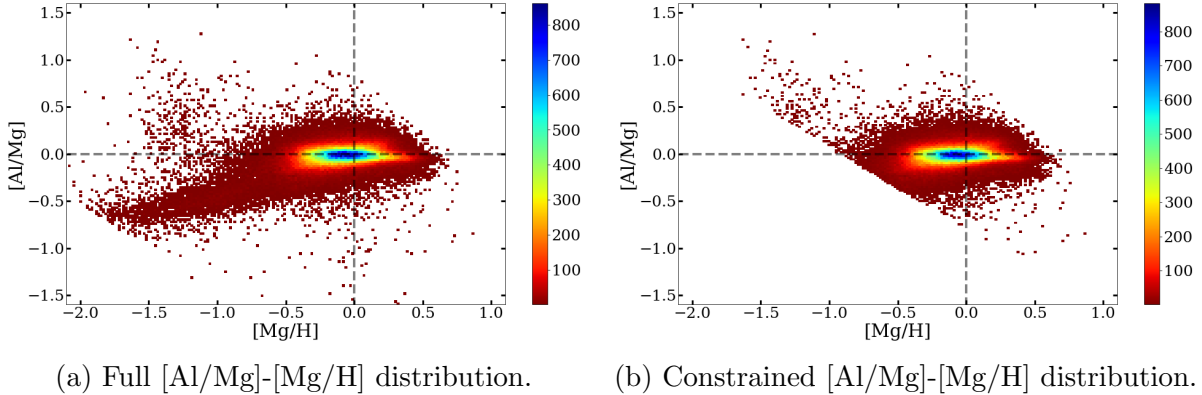
Figure 2.3: Figure (a) shows the full distribution of [Al/Mg] with [Mg/H], whereas (b) shows the constrained distribution.

(a) Excluded stars   (b) Included stars.
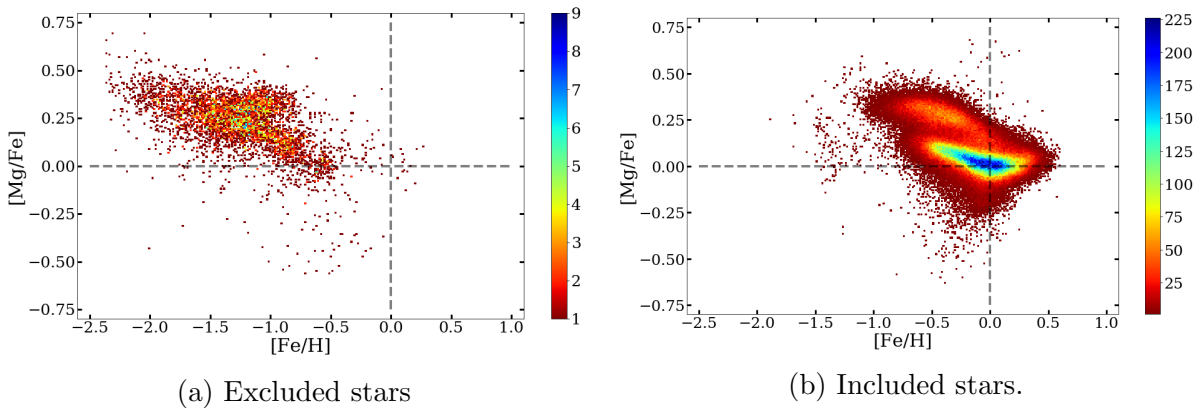
Figure 2.4: The distribution of stars for [Mg/Fe] with [Fe/H]. Figure (a) shows the stars which were excluded with the constraint shown in figure 2.3b, and (b) shows the remaining stars after the constraint was applied.

Furthermore, one wanted to avoid any selection bias, since dwarfs are much fainter than giants at great distances. Through using the effective temperature T_{eff} and logarithmic self-gravity $\log(g)$ from APOGEE DR16, HR-diagrams can be constructed. The HR-diagrams were first used to simply observe if there was any significant difference in the number of dwarf stars at greater distances. It is worth noting that apart from the 7-9 kpc region of the Milky Way, the rest of the remaining sample did not contain a great number of dwarfs, as seen in figure 2.5. This motivates the inclusion of only giants in the sample, to avoid a notable selection bias.

As dwarfs have longer lifetimes, varying ratios of dwarfs versus giants could result in different IMFs. Therefore, only giants were included through constructing a HR-diagram and excluding stars outside the intervals (0 cgs $< \log(g) <$ 4 cgs) and (3500 K $< T_{eff} <$ 5800 K). The effect on the star distribution, when adding this constraint to the [Al/Mg] versus [Mg/H] limit, can be seen in the bottom row of figure 2.6. The most notably affected
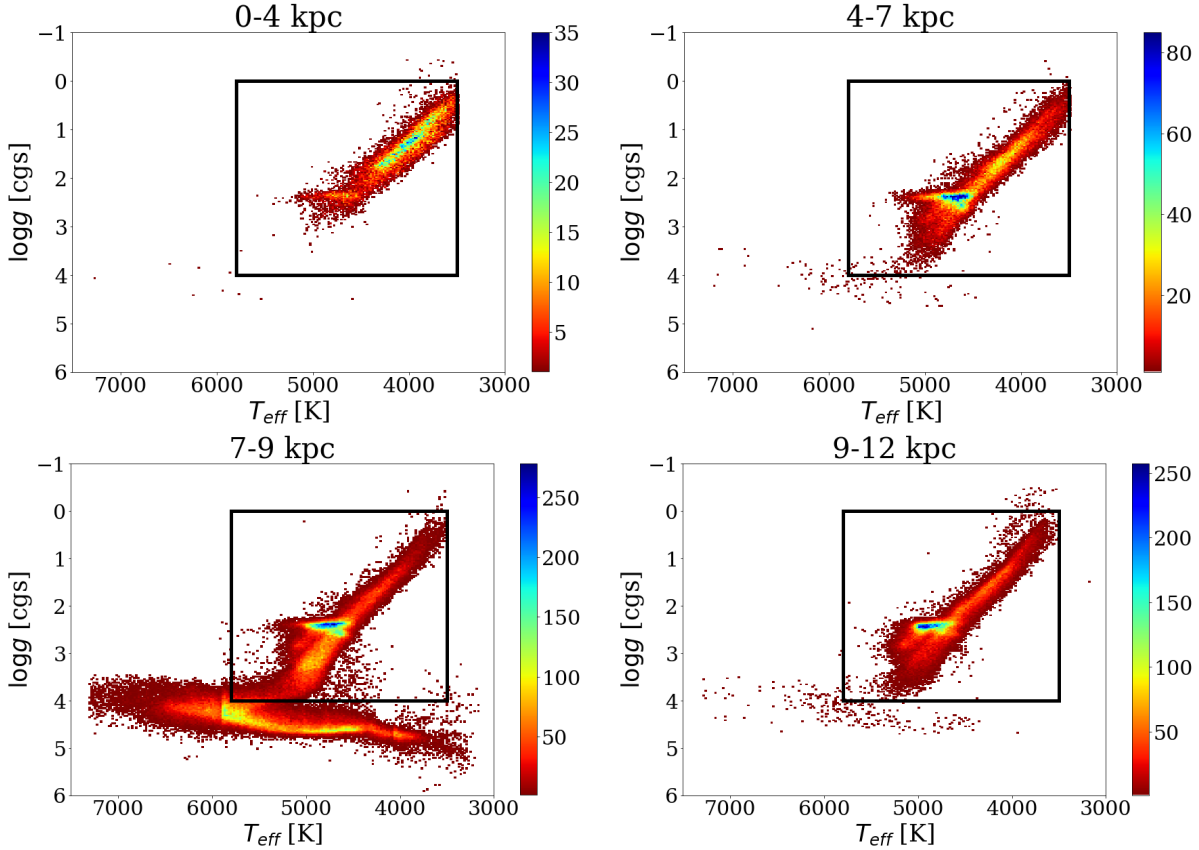
Figure 2.5: HR-diagrams for the stars in the APOGEE DR16 data set in the different galactocentric distance interval (top left) 0-4 kpc, (top right) 4-7 kpc, (bottom left) 7-9 kpc, and (bottom right) 9-12 kpc. The boxes indicate which stars are included when only considering giants, in the intervals (0 cgs < $\log(g)$ < 4 cgs) and (3500 K < T_{eff} < 5800 K).

region is clearly between 7-9 kpc. Again, the effect of this for Si and Ca can be seen in the appendix in figure A.2 and B.2, respectively.

To display the effect the constraints had on the quantity of stars used in the analysis, table 2.1 states how the number of stars decreased in each region after a constraint was applied.
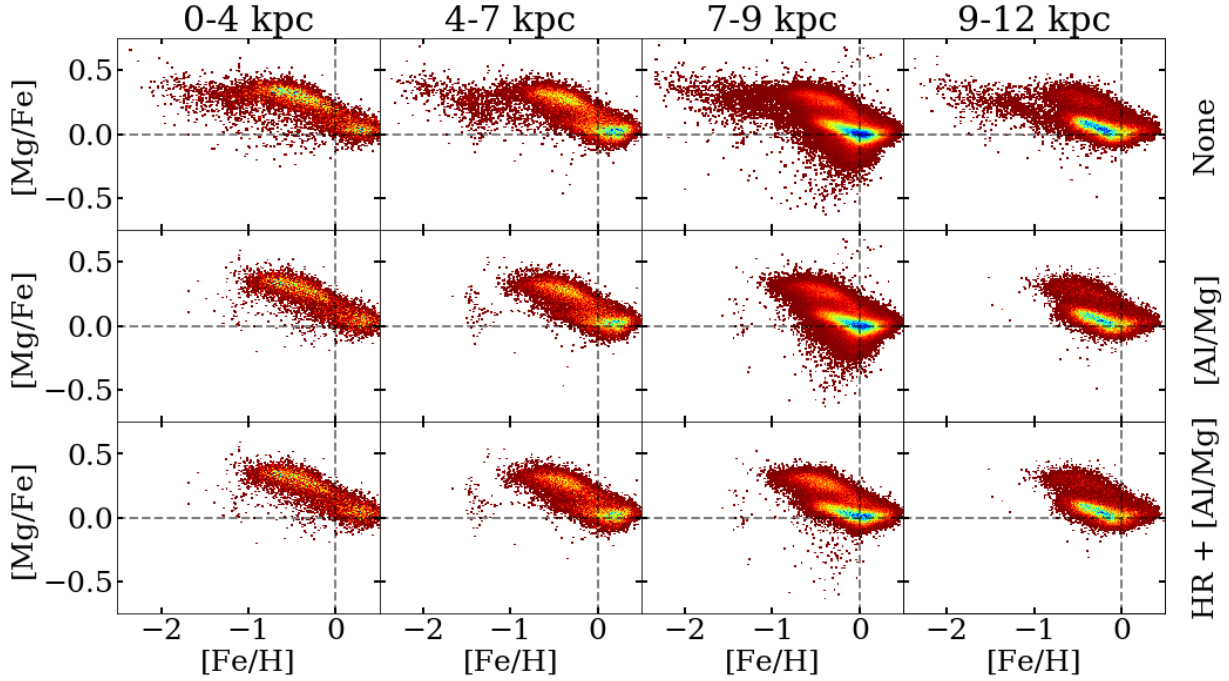
Figure 2.6: The figures show [Mg/Fe] plotted against the metallicity, where the columns from left to right show the galactocentric distances of 0-4 kpc, 4-7 kpc, 7-9 kpc, and 9-12 kpc, respectively. The top row shows the distribution before any constraints are applied, the middle row shows the result of the [Al/Mg]-[Mg/H] constraint (see figure 2.3), and the bottom row only contains giants (see figure 2.5).

Table 2.1: List of number of stars in the varying regions (whole galaxy, 0-4 kpc, 4-7 kpc, 7-9 kpc, and 9-12 kpc) from the APOGEE data set. The table shows how much the number of stars would decrease, as seen in figure 2.6, with each applied constraint.

Constraint	None	[Al/Mg]	[Al/Mg] & Giants
Whole galaxy	203 313	198 003	138 435
0-4 kpc	11 927	10 840	10 808
4-7 kpc	23 386	22 336	22 251
7-9 kpc	118 892	117 111	57 834
9-12 kpc	40 302	39 243	39 086
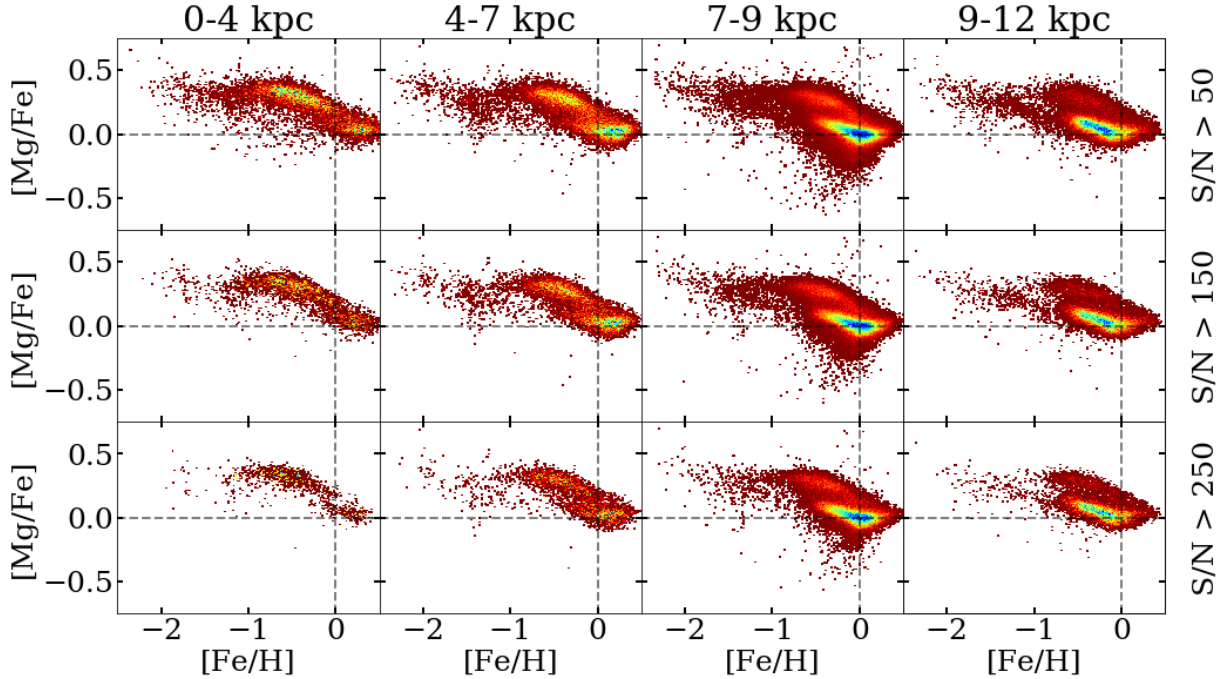
Figure 2.7: Shows the density of [Mg/Fe] versus [Fe/H] at different galactocentric radii and different S/N ratios. From left to right, the figures display 0-4 kpc, 4-7 kpc, 7-9 kpc, and 9-12 kpc respectively. The uppermost figures have an S/N ratio > 50, the middle ones have an S/N ratio > 150, and the bottom ones have an S/N ratio > 250.

The minimum signal-to-noise (S/N) ratio in the sample, after the before-mentioned constraints were applied, was 54, although higher limits were also investigated. The samples for S/N ratio lower limits of 50, 150, and 250, can be seen for [Mg/Fe] at varying galactocentric distances in figure 2.7. It is worth noting that in this figure, none of the previously mentioned constraints have been applied. The numerical impact the different S/N ratios had on the sample for the distance intervals can be found in table 2.2. An increased lower limit for the S/N ratio would decrease the sample size significantly, to the point where some metallicity intervals would not have a single star. An S/N ratio below 50 is bad, which is stated in the data model for APOGEE DR16, and was seen as further motivation for the of S/N ratio minimum of 50 to be sufficient.

As one can see in figure 2.7, the S/N ratio has a considerable impact on the sample size for the 0-4 kpc and 4-7 kpc region. The former is decreased to almost a tenth of its original sample size when a lower limit is set to S/N > 250. The latter region of 4-7 kpc also suffers a great loss, and merely has a fifth of the stars left. These regions are of the smallest sample size, and we would ideally want similar sizes for an accurate comparison.

Table 2.2: List of number of stars in the varying regions (whole galaxy, 0-4 kpc, 4-7 kpc, 7-9 kpc, and 9-12 kpc) from the APOGEE data set, for S/N ratios of 50, 150, and 250.

S/N ratio	50	150	250
Whole galaxy	203 313	121 028	64 048
0-4 kpc	11 927	4 417	1 268
4-7 kpc	23 386	11 085	4 768
7-9 kpc	118 892	72 643	38 486
9-12 kpc	40 302	27 975	16 795

Chapter 3

Tracing the disks' trends

3.1 Metallicity bins
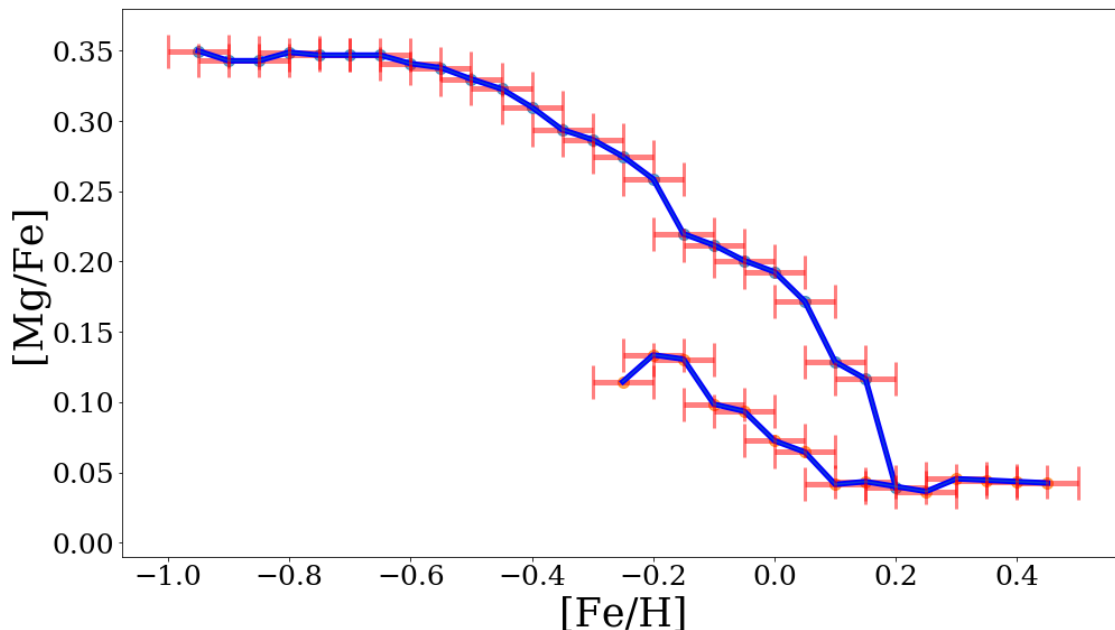
Figure 3.1: Illustration of the α-element abundance trends and the intervals of [Fe/H] used for each data point (red). The trend which is higher in [Mg/Fe] is of the thick disk, and the lower trend is for the thin disk.

To trace the knee of the disks' alpha abundances, for varying galactocentric distance intervals, each point on the knee-trend was spaced 0.05 dex apart in metallicity. These metallicity values overlapped each other, such that they individually spanned an interval of 0.1 dex. An illustration of these intervals is seen in figure 3.1.

The main range of interest was between -1 < [Fe/H] < 0.5, as this is where most stars

reside in figure 2.6. At [Fe/H]≈ 0, the thick and thin disk trends begin to merge, making an analysis focused on the thick disk difficult at higher metallicities. As a greater fraction of stars reside in the thin disk at higher metallicities, as seen in figure 2.6, it created an obstacle for tracing the thick disk successfully.

Similarly, the thin disk is shifted to higher metallicity values and cannot always be traced at low metallicities, unlike the thick disk stars. This is seen clearly in figure 2.6. The 0-4 kpc region hardly has any stars present for the thin disk trend below 0 [Fe/H] dex. The same applies to the interval of 4-7 kpc, although there are more stars with [Fe/H]< 0 than for 0-4 kpc. 7-9 kpc and 9-12 kpc has thin disk trends that stretch for a much longer [Fe/H] interval, though the thick disk trend in the 9-12 region is much weaker compared to its thin disk trend. These factors should be kept in mind when interpreting the results.

3.2   Tracing the trends

To trace the abundance trends of [Mg/Fe] with [Fe/H], generalised Gaussian distributions were constructed. Generalised Gaussian distributions are continuous probability distributions, in our case normal distributions. The peak of a Gaussian is the maximum likelihood estimation, i.e. the value of [Mg/Fe] for a given star. The width of the Gaussian peak is given by the estimated error, such that a wider Gaussian distribution would be the result of a larger uncertainty. In the APOGEE DR16 data set, both the chemical abundances and their respective error are presented. The errors can be used as the standard deviation to construct a Gaussian for each star, using the `norm.pdf` command. These can be summed together to build a generalised Gaussian distribution, which better displays the peak densities of the thick and thin disks.

Occasionally, if few stars were used to construct the generalised Gaussian, a split peak could arise in one of the peaks. An example of how this could look can be seen in the bottom row of the column for the 7-9 kpc interval in figure 3.3. It could be that the two peaks individually belonged to each disks' trend, but in some cases a split peak would arise when the two disks had not merged yet. This would cause the peak of the other disk to be ignored, as they frequently are of different heights at lower and higher metallicities. To avoid these errors, the maximum distance between each peak was set to 0.05 [Mg/Fe] dex.

Once the trends of the disks begin to merge, the values of the thick and/or thin disk trends will suffer greater inaccuracies due to this constraint. However, since the primary interest of this study was to trace the individual trends of the disks where they appear the most prominent, this was a necessary sacrifice.

Other issues that arose when finding the peak star density of each disk were the plateaus and uneven Gaussians. Oftentimes, the peaks would appear asymmetric or irregular. For some of the metallicity bins, one would guess that the true maximum would be found slightly shifted from the identified peak. To take this into account proved hard to implement successfully, and was not done. However, the impact that the irregular Gaussians will have on the results, especially for the low star-count intervals, should be kept in mind.

Using the same intervals of metallicity as previously mentioned, the knee itself could then be traced with great accuracy. The [Mg/Fe] values for each disk in the metallicity bins was selected by identifying the two largest peaks in every generalised Gaussian distribution. Examples of these generalised Gaussians for the different galactocentric distance intervals can be seen in figures 3.2-3.3. The figures do not contain Gaussians for overlapping intervals of metallicity, i.e. they are of intervals 0.1 [Fe/H] dex apart.

Figure 3.2: The graphs show the generalised Gaussian distributions for each galactocentric distance and metallicity interval. From left to right are the distances 0-4 kpc, 4-7 kpc, 7-9 kpc, and 9-12 kpc, respectively. The metallicity increases from the topmost row and downwards, starting at -1.0 and ending at -0.2 [Fe/H] dex.
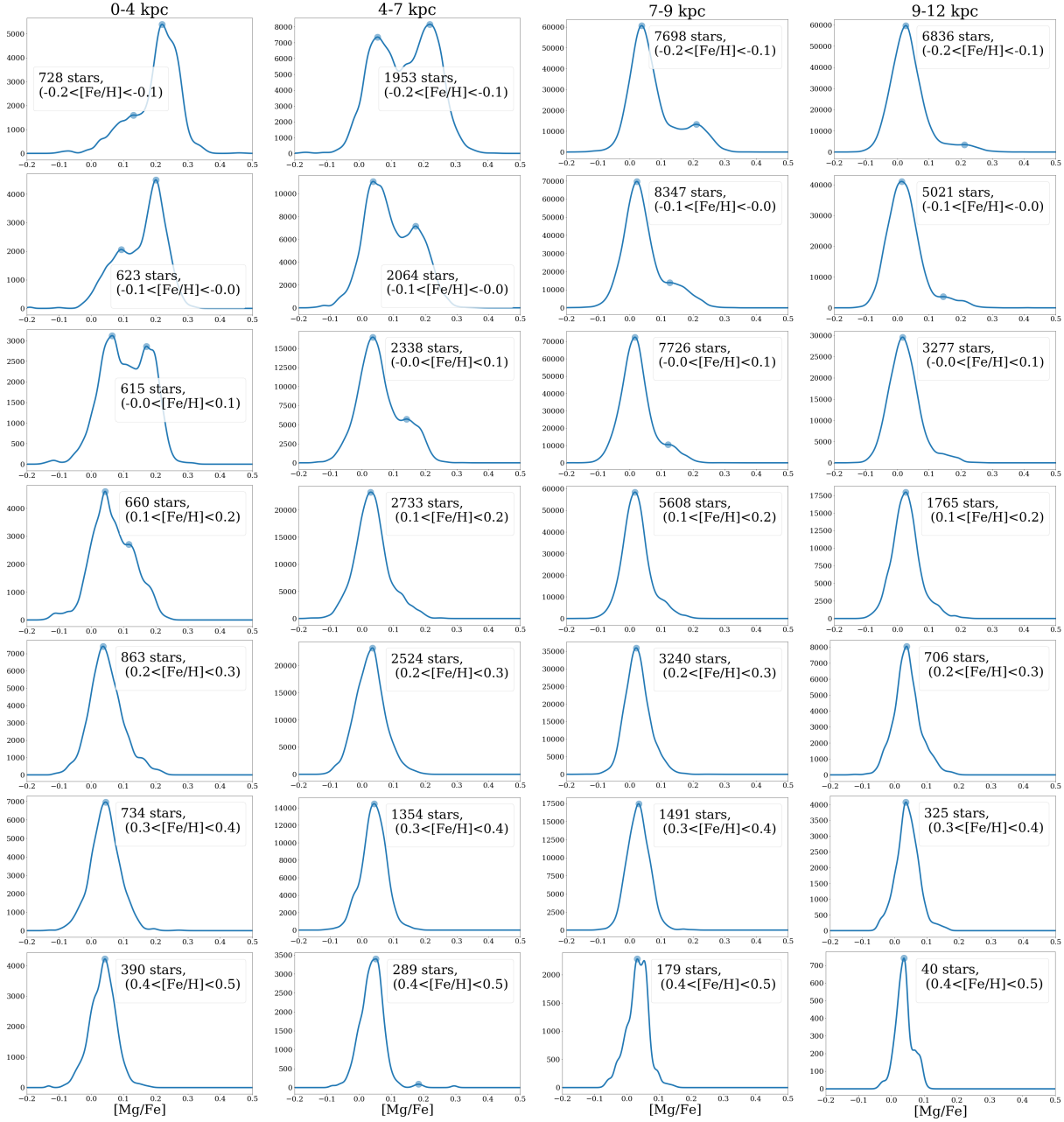
Figure 3.3: Same as figure 3.2, but for (-0.2 < [Fe/H] dex < 0.5).

3.3 Bootstrapping

For the error analysis, an algorithm for bootstrapping was constructed. The purpose of the bootstrapping was to estimate an error for the Mg abundances when tracing the knee. This was done by drawing random stars from the original data set and creating a new sample of 203 313 stars, using the `random.choices` command, where the stars were able to appear multiple times. The errors of the Mg abundances were drawn in such a way too, which meant that a star could now have a different error than in the original sample. Apart from the error of the Mg abundances, the star kept all of its other properties, such as galactocentric distance, [Fe/H], $\log(g)$, and T_{eff}.

Using the same model with the quality flags and constraints mentioned in section 2.1 and 2.2, the abundance trends were traced with a new sample for 500 iterations to compile a mean value and the spread of [Mg/Fe] for each [Fe/H] interval. The result can be seen in figure 3.4. The metallicity intervals where the values suffer larger spreads indicate that the result in these bins could suffer from greater uncertainties because of few stars in the interval.

In figure 3.4 it is worth noting is that unlike all other colour maps in the paper, the density here depends on the number of iterations in the same bin. Furthermore, the colour bar changes slightly with each distance interval. The intervals of 7-9 kpc and 9-12 kpc are shifted to much higher iteration densities than for 0-4 kpc. This means that the bootstrapping of the former distance intervals are of greater precision than the latter.
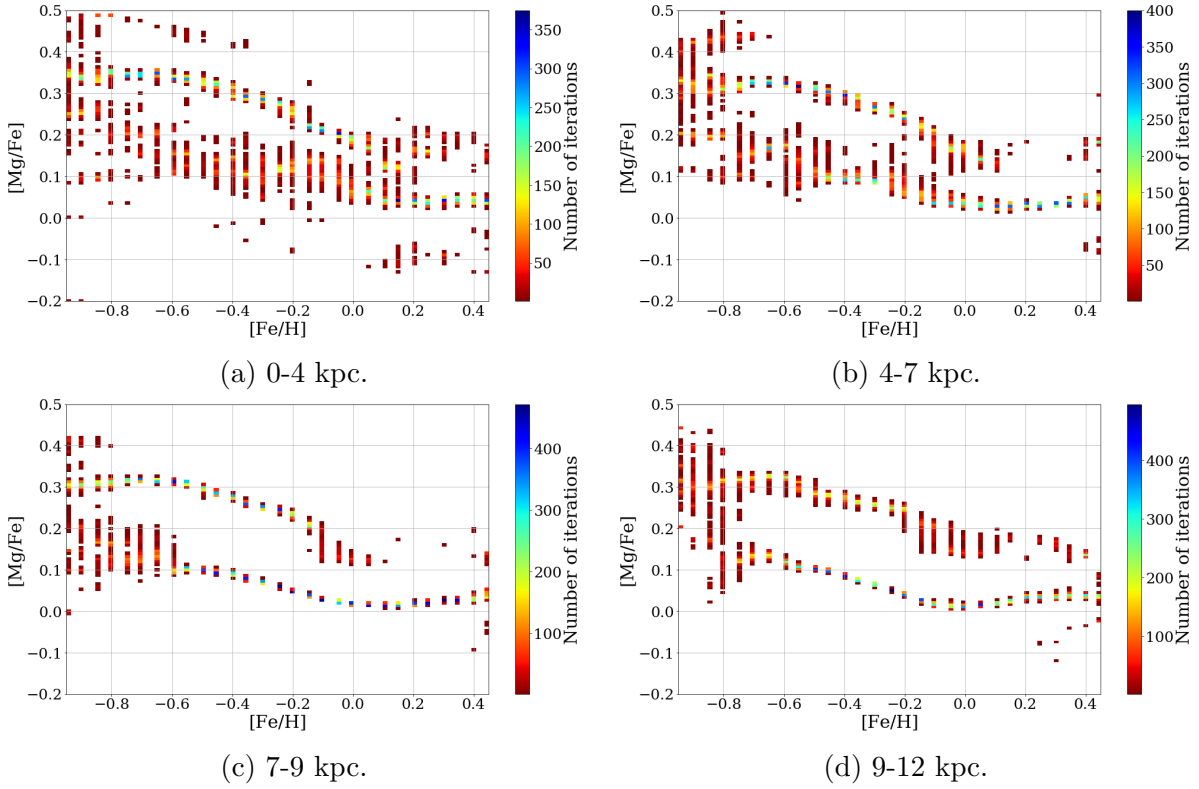
(a) 0-4 kpc.

(b) 4-7 kpc.

(c) 7-9 kpc.

(d) 9-12 kpc.

Figure 3.4: For different distance intervals, the figures show the distribution of [Mg/Fe] in each [Fe/H] bin, for both the thick and the thin disk, after 500 iterations of bootstrapping.

Chapter 4

Results

In figure 4.1a, the results from tracing the [Mg/Fe]-[Fe/H]-abundance trends for the thick and thin disks without any constraints are presented. It contains all stars where values were available in the data set and no quality flags were present. Considerable variations are seen here, and it appears as if the Mg-abundance trends are somewhat elevated for the inner regions of the galaxy, compared to the outermost regions.

Figure 4.1b has only included the stars after constraining the [Al/Mg] trends (see figure 2.3). As seen in figures 2.4 and 2.6, many of the scattered stars have been excluded, and the trends cannot be traced at low metallicities. This is believed to be a more accurate representation of the disks' true trends. However, the tracing of the trends matches those seen in figure 4.1a quite well.

The results from only including giants in the HR-diagram (see figure 2.5) can be seen in figure 4.1c. There are hardly any changes in this result compared to that of figure 4.1a, but we avoid any selection bias which could be present. The trend which is primarily affected is the distance interval of 7-9 kpc. This is reasonable, seeing as many stars were excluded from the HR-diagram in figure 2.5.

The final results of tracing the [Mg/Fe]-[Fe/H]-abundance trends at different galacto-centric radii are shown in figure 4.1d, where both of the before-mentioned constraints have been included.

As previously mentioned, it is worth noting that the thin disk trend is not prominent at low metallicities, as can be seen in the distribution in figure 2.6. Therefore, points lower than $[Fe/H] \approx 0$ for the 0-4 kpc interval suffer great uncertainties and occasionally misrepresent the true trend. The same applies for the 4-7 kpc, 7-9 kpc, and 9-12 kpc intervals below $[Fe/H] \approx -0.4$, $[Fe/H] \approx -0.6$, and $[Fe/H] \approx -0.8$, respectively.
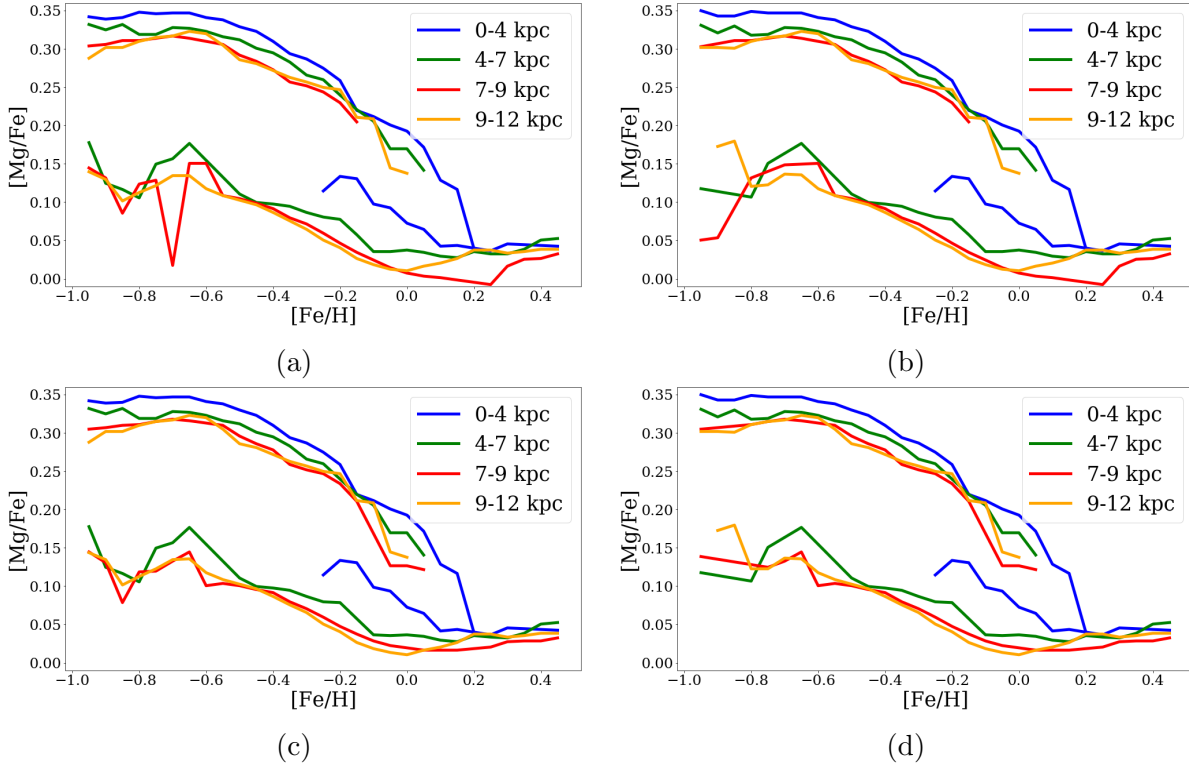
Figure 4.1: The knee traced for the thick and thin disk. (a) has not undergone any constraints, (b) the constraint to [Al/Mg] with [Mg/H] seen in figure 2.3, (c) only including the giants in the black box in figure 2.5, and (d) uses both constraints in (b) and (c).

Bootstrapping was performed for 500 iterations to determine the uncertainty in the position of the knee. Only performing 100 iterations gave almost identically accurate results, but for the sake of a potentially improved error analysis, 500 iterations were completed instead. Although it did not change the mean value trend much, it may have had a significant effect on the distribution spread. In figure 4.2, both the mean trend from the bootstrapping values and the final result from figure 4.1d are shown for comparison. Furthermore, the error bars and grey area show the distribution spread of [Mg/Fe] for each [Fe/H] bin, determined from the standard deviation. The error analysis shows that the results found from the original data neatly align with the bootstrapping results, in the metallicity intervals where the thin disk and thick disk are prominent. As expected, the spread is much larger in regions where the disks are not traceable in the original analysis.

All the distance interval's mean trends from the bootstrapping are included in figure 4.3, where it is evident that they generally match the results in figure 4.1d well. Once the two disks begin to merge, accurate values for the trends were difficult to obtain, as these metallicity intervals oftentimes resulted in irregular Gaussians.
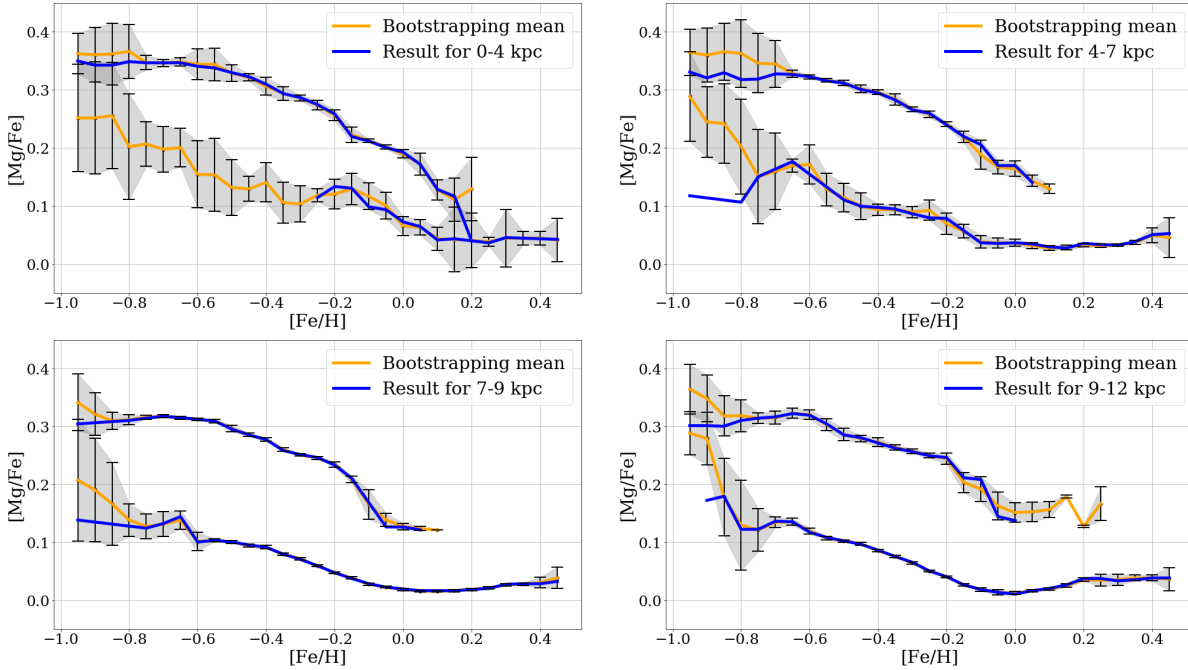
Figure 4.2: Comparison between the bootstrapping mean trend and the analysis result for the different galactocentric distance intervals.
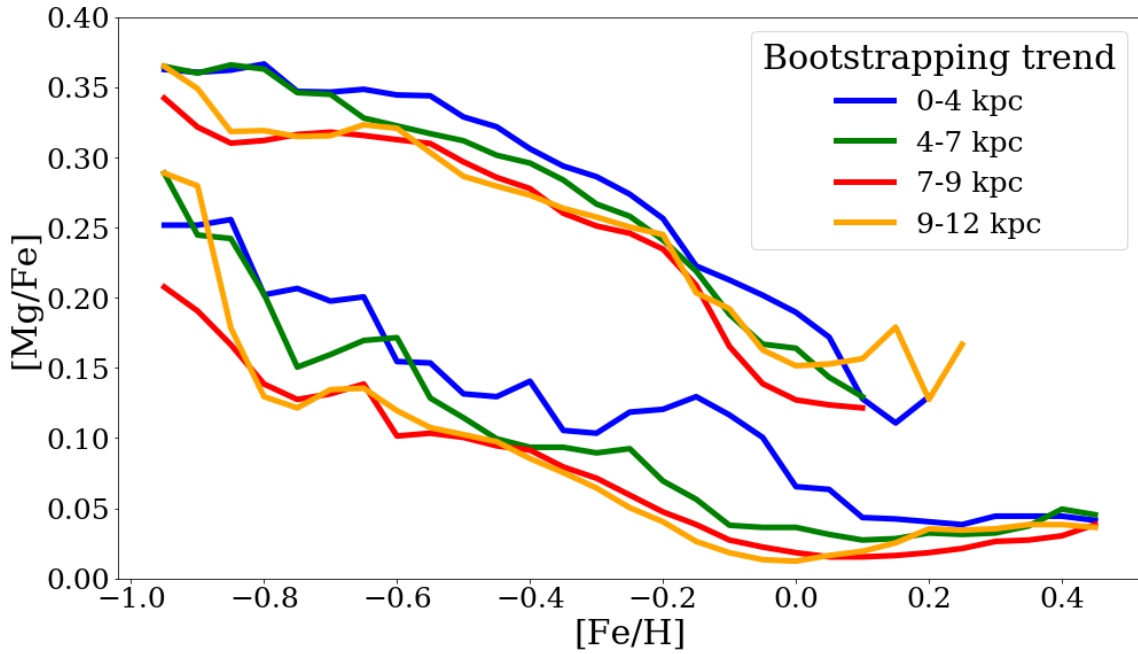
Figure 4.3: The knee traced for the thick and thin disk using the mean value for each point after 500 iterations of bootstrapping.
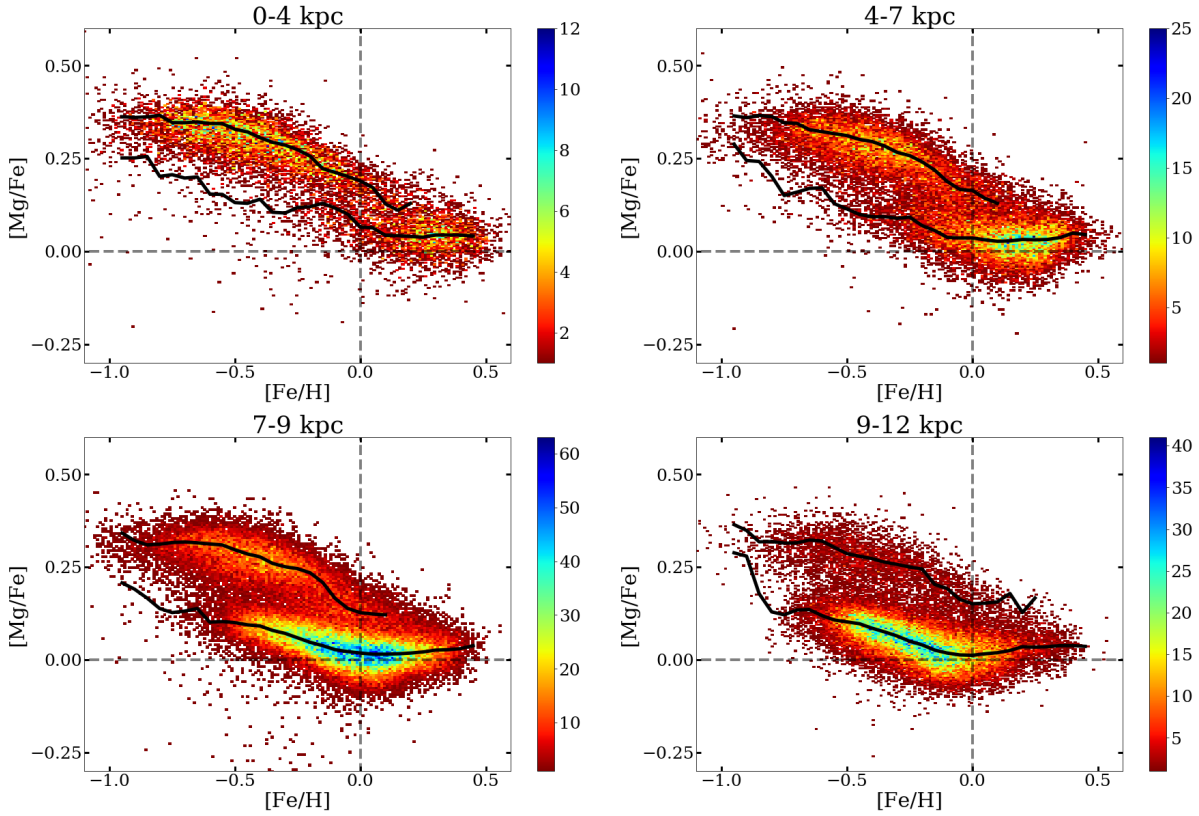
Figure 4.4: Comparison between the bootstrapping mean trend and the star distribution after both constraints in the model have been applied, as seen in the bottom row of figure 2.6.

In figure 4.4, the bootstrapping mean trend is illustrated with the star distribution of the bottom row in figure 2.6. This checks that the trend agrees with the distribution, and any deviations can be explained by low star-count density.

Chapter 5

Discussion

The main finding of the study was that the abundance trends of [Mg/Fe] with [Fe/H], in fact, appear to be elevated in the inner disk/bulge region compared to the local thick disk. However, it is difficult to determine if the SFR appears higher too. As we use the position where the knee begins as an indication of SFR, it is difficult to pinpoint exactly where this is on the trends. If we determine the shift in the knee by the distance between the slopes instead, the bulge's knee seems shifted by [Fe/H] $\approx$ +0.1 from the local thick disk's knee. This is in agreement with the results of Bensby et al. (2017) and Johnson et al. (2014), where the knee for the bulge was found to shift [Fe/H] $\approx$ +0.1 and [Fe/H] $\approx$ +0.1 − 0.2, respectively, compared to the local thick disk. Rojas-Arriagada et al. (2017) determined the shift at [Fe/H] $\approx$ +0.06, but with an upper limit of 0.24 [Fe/H] dex, which means that the results found here are within the range of previous estimates.

As the knee is an indication of SFR (see figure 1.1), our result implies that the SFR could vary with galactocentric radius in the thick disk of our galaxy. This, as mentioned in the introduction, would be in line with the fact that the gas density in our galaxy radially decreases. The SFR should be roughly proportional to the gas density squared (Schmidt 1959). However, what factors have contributed to the SFR we see today is still an interesting point of discussion.

As proposed by Barbuy et al. (2018), an elevated plateau for α-element abundances, along with a knee shifted to higher metallicities, can be used to assess the star formation history (SFH) of galactic components. As both of these are seen to be elevated in the bulge region compared to the local thick disk, this might be an indication that the bulge is not merely a superposition of a thick disk, thin disk, bar, and halo components. The bulge could instead be a separate component of the Milky Way, with its own stellar population.

The stellar populations in the Milky Way can reflect on the chemical composition in different regions of our galaxy, at their time of formation. How the star formation varies can provide insight into the history and evolution of our galaxy (Cole et al. 2007; Gallart et al. 2015; González Delgado et al. 2015, 2016; Beasley et al. 2015). This is easier said than done though since stellar motions can result in radial migration. As stars are likely to move inwards or outwards throughout the galaxy over the course of their lifetime, radial migration could affect the results found in this project. However, which stars undergo this

mechanism is a major field of study on its own, with no clear answers as of yet. Therefore, we can only speculate how it affects the interpreted SFR from the results in this thesis.

The impact of radial migration on the results is difficult to draw any conclusions from. As stars can live for billions of years, and during their lifetime could migrate from their birth location, pinpointing where they originally formed is indeed a challenge. Studies by Quillen et al. (2009), Bekki & Tsujimoto (2011), and Bird et al. (2012) have shown that mergers and perturbations from satellite galaxies can induce radial migration. Since there is evidence that the Milky Way has historically interacted with many satellites, it follows that these could have contributed to the radial migration of stars in our galaxy. Minchev et al. (2013) found that a large fraction of old metal-poor, high-$[\alpha/\text{Fe}]$ stars can reach the solar vicinity from the central region of the Milky Way, as a result of perturbations from high redshift mergers. However, to currently include any potential effects of radial migration on the analysis is outside the scope of this project.

Another factor which may influence the results is the existence of stars originating from satellite galaxies, such as the Gaia-Enceladus dwarf galaxy. The Gaia-Enceladus merger is believed to be the last significant merger that the Milky Way has undergone, estimated to have happened ∼10 Gyr ago. The debris from the merger has been found to make up a large fraction of the inner stellar halo (Helmi et al. 2018), and the merger is believed to have had a significant influence on the disk as well. However, the effects on the disk are still unknown (Gallart et al. 2019).

The two constraints utilised in the model removed a lot of the background noise and created a distinct final distribution, illustrating the thin and thick disk trends, as seen in figure 2.6. The exclusion of stars from the [Al/Mg]-[Mg/H] distribution cleared out much of the scatter at low metallicities. Furthermore, the inclusion of only giants removed a significant portion of the other scattered stars and ensured a lower selection bias. This was a rather crucial constraint, as the local disk (7-9 kpc) had an abundance of dwarfs compared to the other regions. Dwarfs are intrinsically fainter and are thus far more difficult to observe at great distances. The inclusion of only giants hardly affected regions other than the solar neighbourhood, as is seen in table 2.1 and figure 2.5.

Large uncertainties are present in the thin disk's trends at low metallicities, which is seen in figure 4.2. This can be explained easily by the fact that the thin disk has not yet become prominent before higher [Fe/H] values are reached, which are individual for each distance interval. After that, the mean value trend from the bootstrapping aligns nicely with the results from the analysis of the true data.

Many of the deviating points on the trends for the 0-4 kpc distance interval seen in figure 4.1d can be explained by the generalised Gaussian distributions constructed to trace the knee. As mentioned in section 2.2, some Gaussian distributions appear irregular and the true value of the peak is likely shifted as a consequence of this. The irregularity mainly occurs whenever there is a low star-count in a metallicity bin, as seen in figures 3.2-3.3. Seeing as the 0-4 kpc region generally has the lowest sample size, it follows that it was heavily affected by this. However, we also see that this affects other distance intervals in the metallicity bins where the star-count is low, and sometimes even when the star-count is relatively high.

Furthermore, some Gaussians have a split peak, where the true maximum likely resides between the two peaks. A method in the algorithm is needed to work around this, which would take into account the overall shape of the generalised Gaussian distribution. Using bootstrapping as a form of error analysis seems to be a successful method of circumventing this. The Mg-abundance trends neatly aligned in figure 4.3, and appear to accurately represent the peak densities of the star distributions in figure 4.4.

With and without the applied constraints, the IMF appears higher at shorter galactocentric distances. The two constraints in this study, individually, seemed to result in roughly the same IMF as before they were applied. When using the same constraints for the bootstrapping, the SFR knee's position is nearly identical with the results of the analysis, for all four investigated galactocentric regions. The trends in the error analysis deviate, as previously mentioned, when the star density distribution declines at the upper and lower limits of [Fe/H] for each distance interval and disk.

For the region between 7 and 9 kpc, which is the area in which the Sun resides, the bootstrapping mean trend and the analysis result agree well (see figure 4.2). A reason why they do is likely due to the large sample size in this region. As seen in table 2.1, the number of stars residing between 7 and 9 kpc is larger than for 9 to 12 kpc. However, the former interval of only 2 kpc contains more than the 9-12 kpc region, which stretches 1 kpc further. This is a direct consequence of observational bias, since the APOGEE survey can observe many more, as well as fainter, stars in the solar neighbourhood. This can also clearly be seen in figure 2.1, where the peak star density is in the solar vicinity.

Although the SFR and IMF were implied to possibly vary for the distance intervals 0-4 kpc, 4-7 kpc, 7-9 kpc, and 9-12 kpc, this study did not look at greater galactocentric distances. These could potentially show another shift in the abundance trends, indicating a different SFR and IMF. However, the study wished to focus the analysis on whether the abundance trends differed between the bulge and the thick disk. As previous studies have also found indications that the bulge has elevated α-enhancement levels compared to the local thick disk (Bensby et al. 2017; Bensby et al. 2013; Johnsson et al. 2014; Jönsson et al. 2017; Rojas-Arriagada et al. 2017), this project aimed to bring more clarity to the matter. Furthermore, the thick disk would be difficult to trace after 12 kpc, seeing as the 9-12 kpc interval has a much greater abundance of thin disk than thick disk stars. The remaining sample size, as seen in table 2.1, only has roughly 10 000 stars. Although this sample size is sufficient to trace the thick disk for the 0-4 kpc interval, the bulge region contains a much greater ratio of stars residing in the thick disk relative to the thin disk.

Since Mg is just one α-element, it would be of interest to investigate others too. An element such as Si (see figure A.1 and A.2) also shows elevated levels for the bulge region, as seen in figure A.3. However, Si does not possess a knee as steep as Mg does and the results suffered greater variations than those of Mg. Some elements, such as Ca (see figure B.1 and B.2), are much more complicated to trace the individual disks' trends for, seeing as they are less distinguishable from one another. Ca was also attempted to be traced, and the result of this is seen in figure B.3. As the two disks overlap to a greater extent than for Si and Mg, it is challenging to draw any conclusion from these results. Thus, Mg's distinct trends for both disks and prominent knee in the thick disk simplified the analysis.

Chapter 6

Conclusions

To summarise, the project investigated the abundance trends of [Mg/Fe] with [Fe/H] in different galactocentric distance intervals. We found that the position of the knee appeared constant for the different regions of the Milky Way, although this is difficult to say for sure since the knee is challenging to pinpoint. However, if one uses the slope after the knee instead, it seems to shift to higher metallicities in the bulge region compared to the local thick disk. This implies that the SFR could have been higher in the bulge region, which has been indicated by other studies (Bensby et al. 2013, 2017; Johnsson et al. 2014; Jönsson et al. 2017; Rojas-Arriagada et al. 2017).

The exact shift of the slope after the knee was difficult to determine, but was roughly [Fe/H]$\approx +1.0$, in accordance with previous studies. Moreover, the results also found that the IMF appears larger in the bulge and inner galactic regions. Both of these results, when combined, might indicate that the bulge and thick disk are two different components and that the bulge is not solely a superposition of components of the thick disk, thin disk, halo, and bar. Instead, it could be a separate population.

The implied SFR from the results could have been affected by mechanisms such as radial migration. However, to investigate that mechanism's influence on the results is outside the scope of this project. The findings could have also been impacted by the debris from past mergers, and this was attempted to be taken into account with the constraints.

Delightfully, the bootstrapping error analysis found that the trends for the thick and thin disks aligned well with the results found from the true data sample. The spread was smallest for the 7-9 kpc region, as this interval has the largest star-count. Furthermore, we see greater variations in the bootstrapping mean trend and spread where the disks are not prominent, as expected.

For future studies and improvements, it would be interesting to investigate other α-elements in an efficient manner. Apart from Mg, the α-elements Si and Ca were also traced, as can be seen in appendix A and B, figures A.3 and B.3. Although far more difficult to trace, the results for Si also indicate elevated α-enhancement levels in the bulge region than in the local thick disk. However, the thick disk is not as distinguishable for Ca and the trends are much more difficult to interpret.

Furthermore, it would be useful to fit trend-lines for the α-abundances to accurately

determine separation in $[\alpha/\text{Fe}]$ and $[\text{Fe/H}]$ between the distance intervals. Seeing as the α-abundance trends are quite irregular, this would simplify the interpretation of results.

Moreover, a direct way to improve the results in figure 4.1 would be to find a way to handle the irregular or split-peak Gaussian distributions. This would hopefully lead to abundance trends with fewer variations and a more accurate representation of the knee.

Acknowledgements

Bibliography

Adibekyan, V. Zh., Santos, N. C., Sousa, S. G., & Israelian, G. 2011, A&A, 535, 11

Arnone, E., Ryan, S. G., Argast, D., Norris, J. E., & Beers, T. C. 2005, A&A 430, 507

Bailer-Jones, C. A. L., Rybizki, J., Fouesneau, M., Mantelet, G., & Andrae, R. 2018, AJ, 158, 58

Barbuy, B., Chiappini, C., &, Gerhard, O. 2018, ARA&A, 56, 223

Beasley, M. A., San Roman, I., Gallart, C., Sarajedini, A., & Aparicio, A. 2015, MNRAS, 451, 3400

Bekki, K., & Tsujimoto, T. 2011, ApJ, 738, 4

Bensby, T., Yee, J. C., & Feltzing, S., et al. 2013, A&A, 549, A147

Bensby, T., Feltzing, S., & Oey, M. S. 2014, A&A, 562, A71

Bensby, T., Feltzing, S., & Gould, A., et al. 2017, A&A, 605, A89

Bird, J. C., Kazantzidis, S., & Weinberg, D. H. 2012, MNRAS, 420, 913

Bland-Hawthorn, J., & Gerhard, O. 2016, ARA&A, 54, 529

Bovy, J., Rix, H.-W., & Hogg, D. W. 2012, ApJ, 751, 131

Cole, A. A., Skillman, E. D., Tolstoy, E., et al. 2007, ApJ, 659, L17

Edvardsson, B., Andersen, J., Gustafsson, B., Lambert, D. L., Nissen, P. E., & Tomkin, J. 1993, A&A, 275, 101

Gaia Collaboration, Brown, A. G. A., Vallenari, A., et al. 2018, A&A, 616, A1

Gallart, C., Monelli, M., Mayer, L., et al. 2015, ApJ, 811, L18

Gallart, C., Bernard, E. J., Brook, C. B., et al. 2019, NatAs, 3, 932

González Delgado, R. M., García-Benito, R., Pérez, E., et al. 2015, A&A, 581, A103

González Delgado, R. M., Cid Fernandes, R., Pérez, E., et al. 2016, A&A, 590, A44

Helmi, A., Babusiaux, C., Koppelman, H. H., et al. 2018, Natur, 563, 85

Hiroyuki, N. & Yoshiaki, S. 2016, PASJ, 68, 5

Johnson, C. I., Rich, R. M., Kobayashi, C., Kunder, A., & Koch, A. 2014, AJ, 148, 67

Jørgensen, B.R. & Lindegren, L. 2005, A&A, 436, 127

Jönsson, H., Ryde, N., Schultheis, M., & Zoccali, M. 2017, A&A, 598, A101

Lee, Y. S., Beers, T. C., & An, D., et al. 2011, ApJ, 738, 187

Liu, C. & van de Ven, G. 2012, MNRAS, 425, 2144

McWilliam, A. 1997, ARA&A, 35, 503

Minchev, I., Chiappini, C., & Martig, M., 2013, A&A, 558, A9

Quillen, A. C., Minchev, I., Bland-Hawthorn, J., & Haywood, M. 2009, MNRAS, 397, 1599

Rojas-Arriagada, A. et al. 2017, A&A, 601, A140

SDSS-IV Collaboration, 2019, astro-ph.GA, submitted, arXiv:1912.02905

Snaith, O., Haywood, M., Di Matteo, P., Lehnert, M. D., Combes, F., Katz, D., & Gómez, A. 2014, A&A, 578, A87

Schmidt, M. 1959, ApJ, 129, 243

Appendix A

Silicon
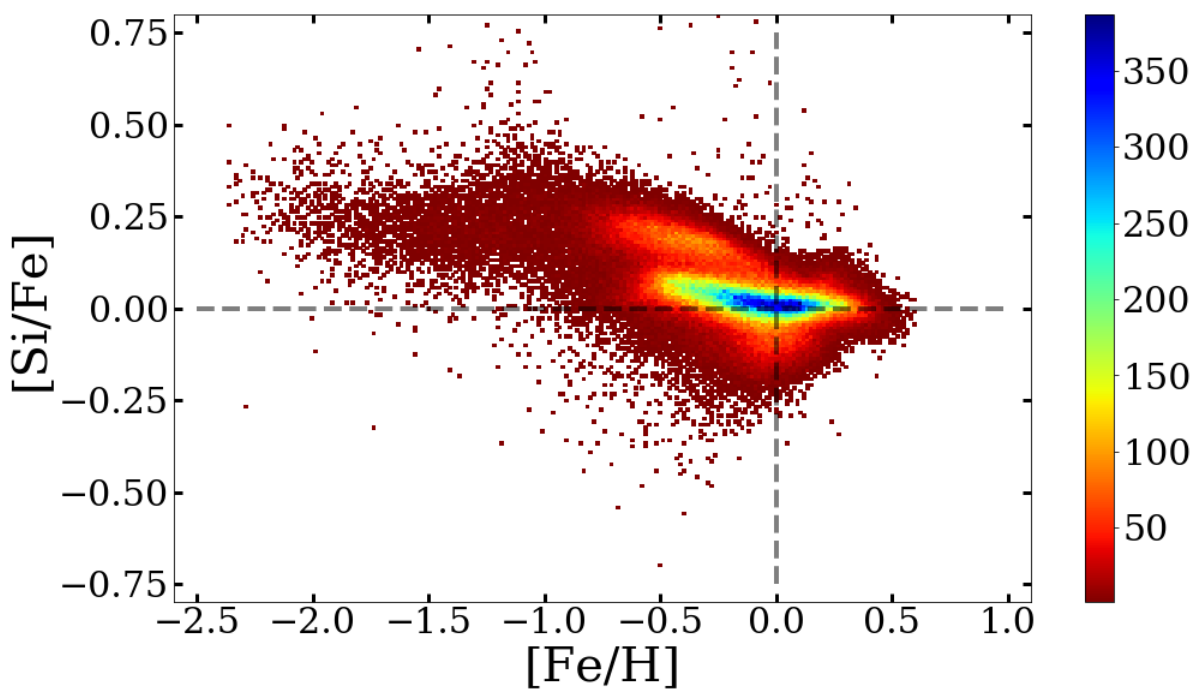

Figure A.1: The star distribution for [Si/Fe] versus [Fe/H] for the 203 313 stars in the sample.
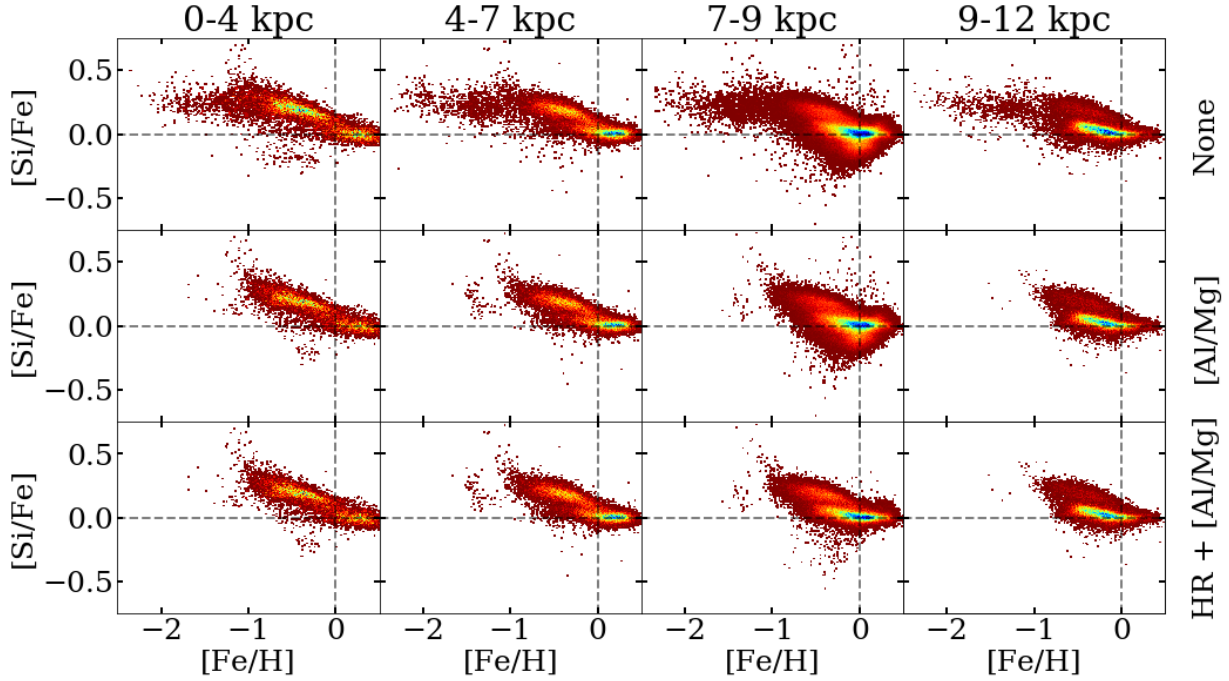
Figure A.2: The figures show [Si/Fe] plotted against the metallicity, where the columns from left to right show the galactocentric distances of 0-4 kpc, 4-7 kpc, 7-9 kpc, and 9-12 kpc, respectively. The top row shows the distribution before any constraints are applied, the middle row shows the result of the [Al/Mg] versus [Mg/H] constraint (see figure 2.3), and the bottom row only contains giants (see figure 2.5).
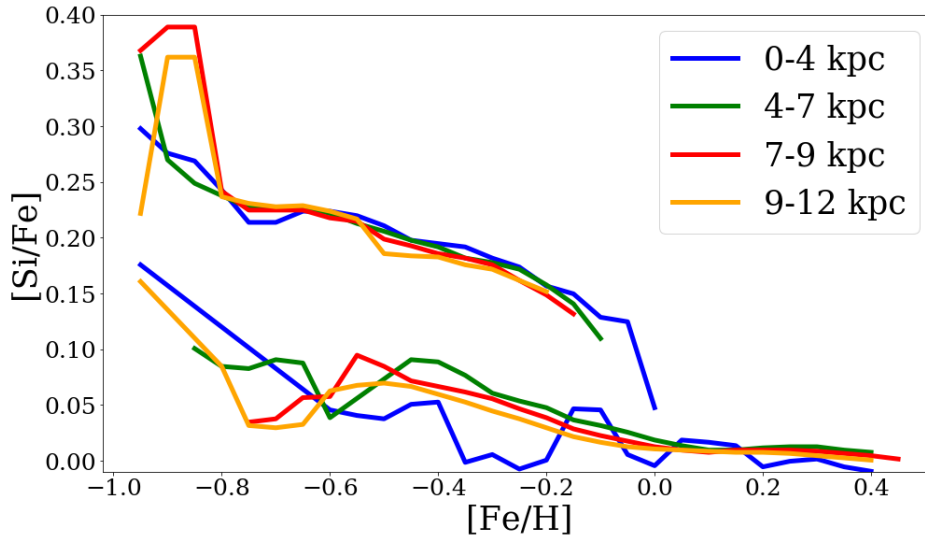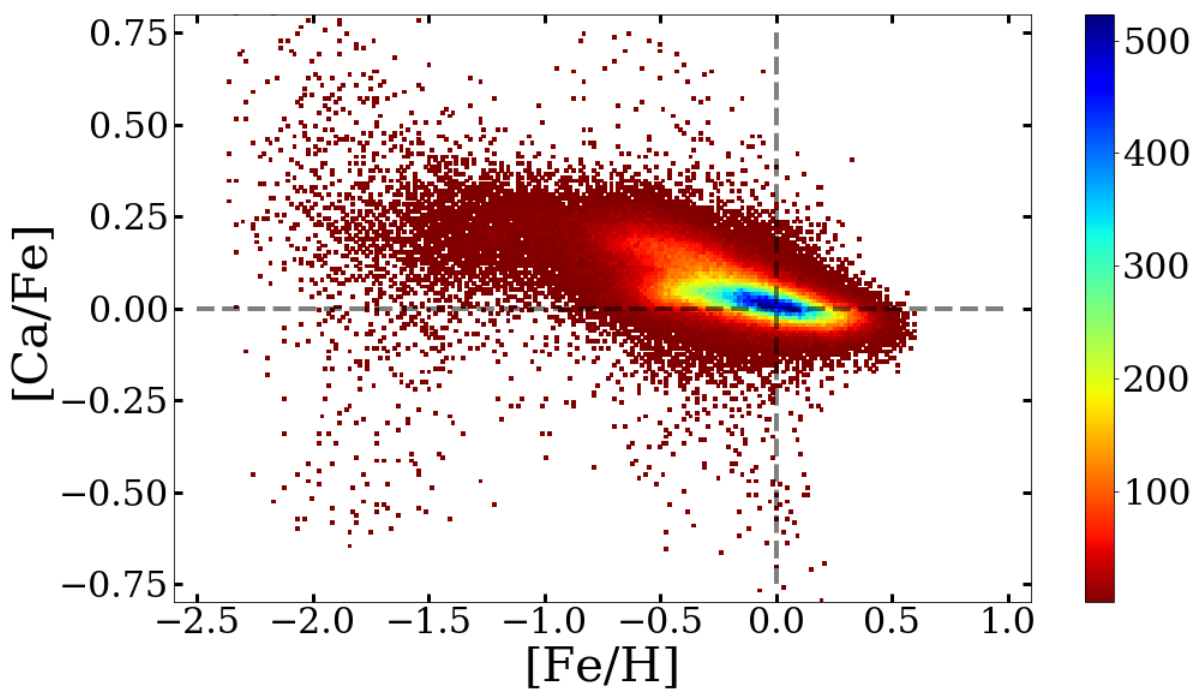

Figure A.3: The SFR knee of Si traced for the thick and thin disk, using both constraints to [Al/Mg] with [Mg/H] and exclusion of dwarfs.

Appendix B

Calcium

Figure B.1: The star distribution for [Ca/Fe] versus [Fe/H] for the 203 313 stars in the sample.
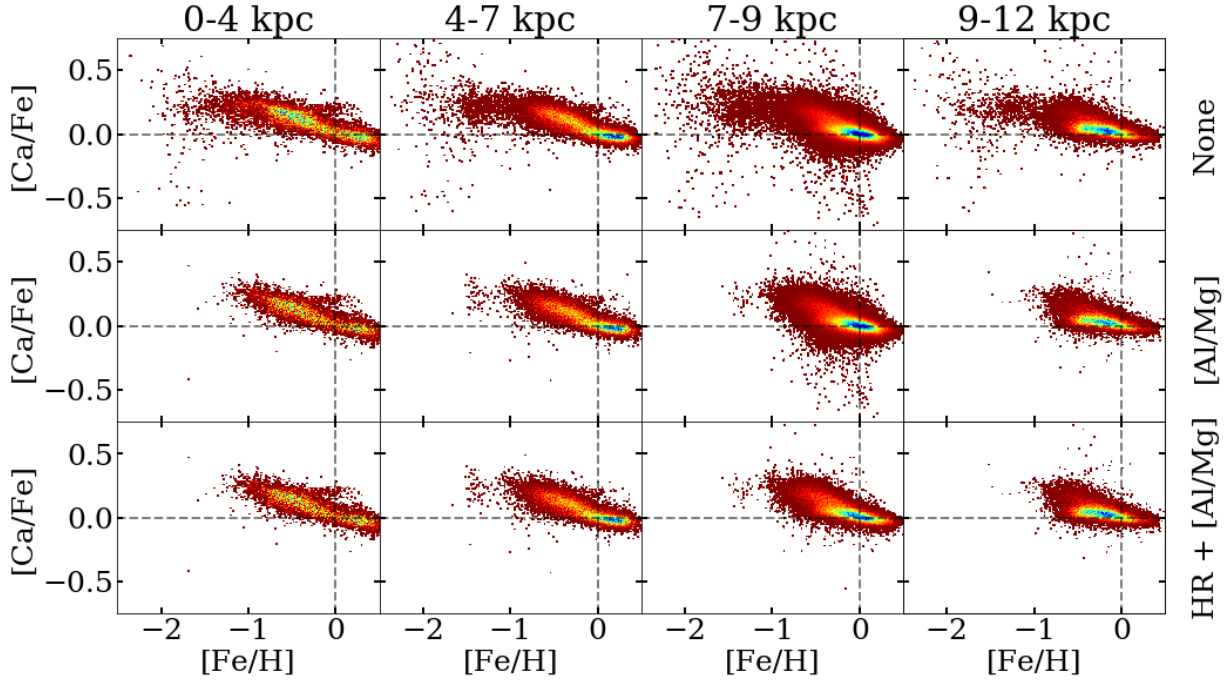
Figure B.2: The figures show [Ca/Fe] plotted against the metallicity, where the columns from left to right show the galactocentric distances of 0-4 kpc, 4-7 kpc, 7-9 kpc, and 9-12 kpc, respectively. The top row shows the distribution before any constraints are applied, the middle row shows the result of the [Al/Mg] versus [Mg/H] constraint (see figure 2.3), and the bottom row only contains giants (see figure 2.5).
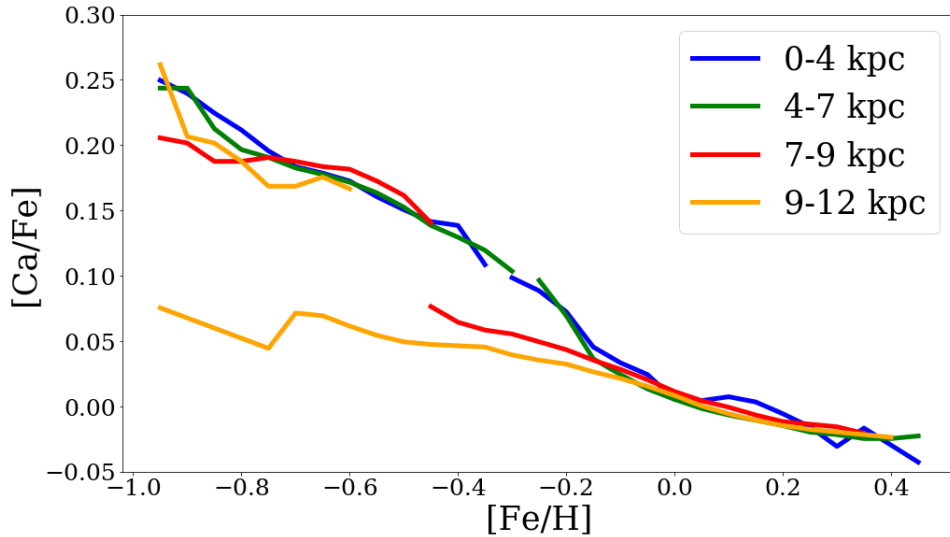

Figure B.3: The SFR knee of Ca traced for the thick and thin disk, using both constraints to [Al/Mg] with [Mg/H] and exclusion of dwarfs.